



HAL
open science

Large scale cavity dissolution: From the physical problem to its numerical solution

Haishan Luo, Farid Laouafa, Gérald Debenest, Michel Quintard

► **To cite this version:**

Haishan Luo, Farid Laouafa, Gérald Debenest, Michel Quintard. Large scale cavity dissolution: From the physical problem to its numerical solution. *European Journal of Mechanics - B/Fluids*, 2015, 52, pp.131-146. 10.1016/j.euromechflu.2015.03.003 . hal-01348512

HAL Id: hal-01348512

<https://hal.science/hal-01348512>

Submitted on 27 Jul 2016

HAL is a multi-disciplinary open access archive for the deposit and dissemination of scientific research documents, whether they are published or not. The documents may come from teaching and research institutions in France or abroad, or from public or private research centers.

L'archive ouverte pluridisciplinaire **HAL**, est destinée au dépôt et à la diffusion de documents scientifiques de niveau recherche, publiés ou non, émanant des établissements d'enseignement et de recherche français ou étrangers, des laboratoires publics ou privés.



Open Archive TOULOUSE Archive Ouverte (OATAO)

OATAO is an open access repository that collects the work of Toulouse researchers and makes it freely available over the web where possible.

This is an author-deposited version published in: <http://oatao.univ-toulouse.fr/>
Eprints ID : 15901

To link to this article : DOI:10.1016/j.euromechflu.2015.03.003
URL : <http://dx.doi.org/10.1016/j.euromechflu.2015.03.003>

To cite this version :

Luo, Haishan and Laouafa, Farid and Debenest, Gérald and Quintard, Michel *Large scale cavity dissolution: From the physical problem to its numerical solution*. (2015) European Journal of Mechanics - B/Fluids, vol. 52. pp. 131-146. ISSN 0997-7546

Any correspondence concerning this service should be sent to the repository administrator: staff-oatao@listes-diff.inp-toulouse.fr

Large scale cavity dissolution: From the physical problem to its numerical solution

Haishan Luo^{a,b,c,d}, Farid Laouafa^{d,*}, Gérald Debenest^{a,b,c}, Michel Quintard^{a,b,c,e}

^a Université de Toulouse, Allée Camille Soula, F-31400 Toulouse, France

^b INPT, UPS, Allée Camille Soula, F-31400 Toulouse, France

^c IMFT (Institut de Mécanique des Fluides de Toulouse), Allée Camille Soula, F-31400 Toulouse, France

^d Institut National de l'Environnement Industriel et des Risques, Parc technologique d'ALATA BP2, F-60550 Verneuil-en-Halatte, France

^e CNRS, F-31400 Toulouse, France

A B S T R A C T

Dissolution of underground cavities by ground water (or solutions) may cause environmental problems and geological hazards. Efficient modeling and numerical solving of such phenomena are critical for risk analysis. To solve the cavity dissolution problems, we propose to use a porous medium based local non-equilibrium diffuse interface method (DIM) which does not need to track the dissolution fronts explicitly as the sharp front methods (such as ALE). To reduce the grid blocks when using the DIM method, an adaptive mesh refinement (AMR) method is used to have higher resolutions following the moving fronts. An efficient fully implicit scheme is used by taking care of the velocities across the gridblock interfaces on the AMR grid. Numerical examples of salt dissolution under different flow conditions were performed to validate the modeling and numerical solving. Core-scale and reservoir-scale cases were carried out to study the mass transport and the evolution of the profiles of the dissolution fronts. Gravity-driven physical instabilities are found to be more strong in the infinite channel with upper and lower planes than in the 3D tube configuration under the same condition. The implementations with the AMR method also showed a very good computational efficiency, while obtaining good agreement with the finest-grid solutions.

Keywords:

Diffuse interface method
Solid-liquid dissolution
Adaptive mesh refinement
Porous medium
Moving interface
Geological hazards

1. Introduction

Cavity dissolution problems are very common in fluid-solid systems, for instance, karstification [1], mining [2], CO₂ storage [3,4], rock weathering by flowing groundwater or other chemical solutions [5,6], etc. In these cases, the growth of underground cavities may cause geological disasters and environmental problems [7–9]; thus, accurate description and prediction of such phenomena are crucial for risk analysis. In this paper, we focus on the study of the evolution of the fluid-solid fronts caused by dissolution, e.g., water flushing the halite deposit. Two types of cavities exist in the nature: (i) a region within a porous medium in which the soluble material has been dissolved, leaving a cavity formed of insoluble material with a large porosity; (ii) a true void cavern space created by the dissolving liquid into a purely soluble solid domain.

The type (i) cavity dissolution may be modeled by a macro-scale porous medium theory involving averaged equations and effective properties. Porous media dissolution models have been introduced and used widely on a heuristic basis. A thorough derivation may be achieved by using mathematical upscaling techniques. For example, volume averaging in [10–12] leads to different models, e.g., local equilibrium models, and local non-equilibrium models. In the latter models, the true dissolution front thickness, i.e., the region where porosity varies due to dissolution, is controlled mainly by a mass exchange term [13–16].

The type (ii) cavity dissolution may be modeled using either the sharp front methods [17–19] or the cellular automaton methods [20,21] and the diffuse interface methods [22]. In typical sharp front methods, like for instance those based on the Arbitrary Lagrangian-Eulerian (ALE) framework [17], the position of the interface with zero thickness is explicitly tracked and is part of the mesh boundaries. These methods are often inefficient in some applications, especially when the shape or the evolution in time and space of the interfaces is complex and not smooth, e.g., the peaks with sharp angles [23]. The geometrical singularities

* Corresponding author. Tel.: +33 344556182.

E-mail address: Farid.Laouafa@ineris.fr (F. Laouafa).

induced by differential dissolution can be overcome by using the transport of a phase indicator, like in a Volume Of Fluid (VOF) method [24]. However, in such cases numerical diffusion generates interface diffusion that must be controlled through the use of compressive schemes and reconstruction procedures. Complex mathematical reconstruction may be carried out using Level-set methods [25–27]. In contrary to requiring the special treatment to the interface by the sharp-front methods, the diffuse interface methods (DIM) generate global PDEs for the flow by smoothing the interface as a diffuse layer where some quantities, especially a scalar field that plays the role of the phase indicator, vary rapidly but continuously [28–30]. The continuous nature of the DIM equations solved is certainly an advantage since a dissolution problem can be solved on a fixed grid without a peculiar treatment of the equations in the neighborhood of the dissolution front. This feature is comprehensively discussed in [31], in which a DIM method was proposed based on the local non-equilibrium porous medium theories, such as those originally being used for the type (i) cavity dissolutions, to model the type (ii) cavity dissolutions. It was found out that if the mass exchange term becomes very large, the resulting dissolution front becomes thinner, thus reproducing the kind of sharp dissolution fronts encountered in the purely liquid–solid dissolution problem. Also, after a short transient regime, the thickness of the dissolution front becomes a constant and that the front velocity becomes close to the one of the sharp dissolution interface problem.

Currently, most previous studies on type (ii) dissolutions are limited to pore-scale problems, but few are for large scales. Also, simulations of three-dimensional dissolution cases are rarely in the literature. However, the practical cavity dissolutions are often found with large scales, for instance, large caverns due to dissolution are reported in various countries [32,33], which belong to the type (ii) cavity dissolutions. Therefore, it is desirable for this paper to attempt a study for the modeling of the large-scale cavity dissolution and the efficient numerical simulation of the processes in both time and space. Of course, the DIM models are preferred for numerical implementations because of the continuous nature of the equations. Also, cavities often have locally non-differentiable surfaces which are difficult to be handled with an explicit interface (sharp front) treatment. Nevertheless, inherently to the DIM approaches, the dissolution front is characterized by a strong porosity gradient in the dissolution front area; thus, accurate numerical solutions would require fine grids in the regions where the dissolution fronts are likely to progress. This need for fine grids is also enforced by the fact that the dissolution boundary layer may be thin because of the low liquid diffusion/dispersion coefficient and large length-scale involved. These requirements may lead to the use of quite homogeneous fine grids, thus counter balancing the advantage of DIM. To tackle this limitation, an efficient solution is the use of Adaptive Mesh Refinement (AMR), in which the refinement will take into account, at least, the porosity gradient, in order to follow the dissolution front, and the concentration gradient, to have an accurate estimate of the mass fluxes and hence the dissolution velocity.

The applications of AMR have covered lots of physical problems, such as shock hydrodynamics analysis [34,35], compressible flow [36], turbulent flow [37], flow in porous media [38–40], and oil displacement [41,42]. The AMR methods can be distinguished into two categories: patch-based and cell-based. The patch-based AMR methods solve the problem separately on different patches of the domain under different grid refinement levels, and the solutions are coupled through the interior boundaries using interpolations in space and time [34,43,44]. They are often used to solve the Navier–Stokes equations and hyperbolic equations. The cell-based AMR methods, which are frequently applied to porous media flows [39,42], use one-coupled system (one grid) for all

the grid blocks under different levels. The cell-based methods are efficient when the problems are solved implicitly, because the time step is not so restricted by the size of the fine grid blocks.

In this paper, we use the cell-based AMR for the DIM model with a fully implicit solving, considering that the mass exchange terms have strong impact on all the balance equations and the unknown variables are strongly coupled. We develop a new cell-based AMR algorithm, which is more advantageous to solve fully implicitly the balance equations to ensure the mass conservation. An important aspect of the cell-based AMR is to calculate accurate fluxes across the block interfaces when blocks from different AMR levels are involved. Nevertheless, some of the cell-based AMR algorithms are relatively inaccurate when computing the velocity flux (with Darcy’s Law) across the cell interfaces as the cell-centered nodes of different levels are not along the same straight line. For example, Forsyth and Sammon [41] computed the interface velocity with Darcy’s Law using the pressure (or potential) difference evaluated at two cell-centered nodes, which was pointed out that the truncation error is large. Durbin and Iaccarino [37,39] improved the accuracy using the reconstruction and bi-linear extrapolation of solutions of hanging nodes with anisotropic refinement. It showed globally $O(h^2)$ errors where h represents the characteristic length of the grid block. In this paper, to respect the physical pressure drop along the coarse blocks, we develop an accurate scheme to compute the flux on the interfaces by performing an integration to the pressure along the path between the central and auxiliary points of a coarse block with the help of Darcy’s Law. More details can be found in Section 4.

The paper is organized as follows. First the original dissolution model and the diffuse interface dissolution model based on porous medium theory are introduced briefly, since it has been discussed elsewhere in the literature. Then, the AMR algorithm is presented, the focus being more on the problems specific to dissolution models. Finally, simulation examples are provided which give some insight on the use of DIM–AMR models.

2. Solid–liquid dissolution model

The original mathematical dissolution problem is characterized by the existence of separate fluid and solid phases, denoted by l and s . The solid chemical species dissolves into the fluid phase. As a minimal example, we will consider a single component in the solid phase, denoted A , and a binary mixture in the liquid phase. The total mass balance equation for the liquid phase of density ρ_l flowing at velocity \mathbf{v}_l is written as follows

$$\frac{\partial \rho_l}{\partial t} + \nabla \cdot (\rho_l \mathbf{v}_l) = 0, \quad (1)$$

and the mass balance equation for chemical species A in the liquid phase is

$$\frac{\partial (\rho_l \omega_{Al})}{\partial t} + \nabla \cdot (\rho_l \omega_{Al} \mathbf{v}_l - \rho_l D_{Al} \nabla \omega_{Al}) = 0 \quad (2)$$

where ω_{Al} represents the mass fraction of species A in the liquid phase and D_{Al} is the liquid binary diffusion coefficient.

The mass balance equation for the solid phase of density ρ_s is the following:

$$\frac{\partial \rho_s}{\partial t} + \nabla \cdot (\rho_s \mathbf{v}_s) = 0 \quad (3)$$

where the solid velocity, \mathbf{v}_s , is normally regarded as zero in most cases (in a non moving reference frame).

In the case under consideration, we suppose that the solid dissolution is mainly controlled by thermodynamic equilibrium at the solid–liquid interface. In such a case, this translates into

a simple Dirichlet condition for the species concentration at the solid–liquid interface:

$$\omega_{Al} = \omega_{eq} \quad \text{at } \Gamma_{ls} \quad (4)$$

where ω_{eq} represents the equilibrium mass fraction of species A and Γ_{ls} denotes the solid–liquid interface.

The mass balance for species A at the solid–liquid interface gives:

$$(\rho_l \omega_{Al} \mathbf{v}_l - \rho_l D_{Al} \nabla \omega_{Al}) \cdot \mathbf{n}_{ls} = \rho_s \omega_{As} (\mathbf{v}_s - \mathbf{w}) \cdot \mathbf{n}_{ls} \quad \text{at } \Gamma_{ls} \quad (5)$$

where \mathbf{n}_{ls} represents the normal vector at the liquid–solid interface, and \mathbf{w} the velocity of the interface. The total mass balance at the solid–liquid interface gives:

$$\rho_l (\mathbf{v}_l - \mathbf{w}) \cdot \mathbf{n}_{ls} = \rho_s (\mathbf{v}_s - \mathbf{w}) \cdot \mathbf{n}_{ls} \quad \text{at } \Gamma_{ls}. \quad (6)$$

The problem has to be completed with momentum balance equations, Navier–Stokes equations for instance, and the no-slip boundary condition at the solid–liquid interface gives:

$$\mathbf{v}_l - \mathbf{n}_{ls} \mathbf{n}_{ls} \cdot \mathbf{v}_l = 0 \quad \text{at } \Gamma_{ls} \quad (7)$$

which means that the velocity at the interface is only along the normal direction.

3. Diffuse interface model for the solid–liquid dissolution problem

Luo et al. [31] proposed a DIM method based on the use of a non-equilibrium porous medium theory. The sharp interface solid–liquid problem described in Section 2 is replaced by a porous medium problem where the varying porosity plays the role of a phase indicator, i.e., it gets close to 1 in a pure fluid domain and gets close to zero in a pure solid domain. This DIM method is better understood as the upscaling of the original equations in the framework of a volume averaging theory [12,15]. We briefly present the fundamental results to clarify the notations and concepts and we refer the reader to Luo et al. [31] for further details.

The DIM equations which are written for the upscaling of the mass balances of solid phase, liquid phase, and species A in the liquid phase, can be expressed in the following forms, respectively:

$$-\rho_s \frac{\partial \varepsilon_l}{\partial t} = -\rho_l \alpha (\Omega_{eq} - \Omega_{Al}) \quad (8)$$

$$\frac{\partial \varepsilon_l \rho_l}{\partial t} + \nabla \cdot (\rho_l \mathbf{V}_l) = \rho_l \alpha (\Omega_{eq} - \Omega_{Al}) \quad (9)$$

$$\begin{aligned} \varepsilon_l \rho_l \frac{\partial \Omega_{Al}}{\partial t} + \nabla \cdot (\Omega_{Al} \rho_l \mathbf{V}_l) \\ = \nabla \cdot (\varepsilon_l \rho_l \mathbf{D}_{Al}^* \cdot \nabla \Omega_{Al}) + \rho_l \alpha (1 - \Omega_{Al}) (\Omega_{eq} - \Omega_{Al}) \end{aligned} \quad (10)$$

where ε_l is the volume fraction of the liquid phase, Ω_{Al} is the intrinsic average of the mass fraction, and \mathbf{V}_l is the average of the liquid velocity, Ω_{eq} is the equilibrium mass fraction of species A on the solid–liquid interface, and ρ_l and ρ_s are the liquid and solid densities, respectively. For a binary system (a species and the water), it is easy to define the equilibrium concentration Ω_{eq} by using the saturated concentration. For a system with more than two species, the model and the mass exchange terms become more complicated, depending on the multicomponent equilibrium diagram. Theoretical extensions have been proposed for simple cases such as systems obeying Raoult's or Henry's law [45,46].

The primary unknowns of Eqs. (8)–(10) are ε_l , P_l , and Ω_{Al} , respectively, where P_l is the pressure of the liquid phase. In this DIM model, ε_l plays the role of a phase indicator, the pure liquid phase being represented by $\varepsilon_l = 1$ while the pure solid phase is represented by $\varepsilon_l = 0$. α is the mass exchange coefficient in s^{-1} ,

and it is a function of ε_l . Various expressions have been discussed in [31]. We adopt the following expression:

$$\alpha = \alpha_0 (1 - \varepsilon_l^2) \quad (11)$$

where α_0 is a constant, while many other choices may be taken without changing significantly the solution of the problem. It must also be remembered that these expressions have physical meanings when dealing with true porous media dissolution problems, as illustrated in [15].

For a preliminary study, we use a general model [47] to give the effective diffusion/dispersion coefficient, \mathbf{D}_{Al}^* , which is

$$\mathbf{D}_{Al}^* = \varepsilon_l D_{Al} \mathbf{I} + \frac{\alpha_l}{|\mathbf{V}_l|} \text{diag}(\mathbf{V}_l \otimes \mathbf{V}_l) \quad (12)$$

where D_{Al} is the molecular diffusion coefficient of the species A in the liquid phase l , α_l is the longitude dispersivity, and the operator diag returns the diagonal matrix. The transverse dispersivity is ignored in this expression for simplicity. When Péclet number of the flow is small, the former term is in domination; otherwise, the latter term is significant.

For the momentum balance equation, we adopt a simple porous medium model and the liquid velocity \mathbf{V}_l is calculated using Darcy's law,

$$-(\nabla P_l - \rho_l^* \mathbf{g}) - \mu_l^* \mathbf{K}^{-1} \cdot \mathbf{V}_l = 0 \quad (13)$$

where ρ_l^* and μ_l^* refer to the macro-scale density and dynamic viscosity of the liquid, respectively, and the permeability tensor \mathbf{K} is assumed, for the DIM, as isotropic and obeying the following expression

$$\mathbf{K} = \frac{\varepsilon_l^2 l_c^2}{3} \mathbf{I} \quad (14)$$

where l_c represents the flow characteristic length-scale. Zhao et al. [48] validated the using of Darcy's Law for solid–liquid dissolution problems in the presence of bulk liquid areas, as dissolution is caused mainly by the mass transport around the solid–liquid interfaces. Other choices for the momentum equations are also possible function on the problem under consideration, like Navier–Stokes or Stokes equations with a permeability term, which is used as a penalization term to reproduce the no-flow condition in the solid phase if there is no real porous medium in the problem [49].

According to the discussion in [31], the interface thickness is mainly controlled by the mass exchange coefficient, in particular by the expression in Eq. (11). The mass exchange coefficient can be artificially increased in order to sharpen the interface, but its value should not be too large in order that the dissolution front covers at least two to three grid blocks. This is necessary for the numerical convergence of the scheme. The size of the gridblocks necessary to achieve good accuracy depends on the physical problem under consideration. For instance, if the mass boundary layer is thick, one may accept to increase the thickness of the dissolution zone and hence use coarser grids. However, convective plumes may be initiated within thin boundary layers, thus calling for a fine grid resolution in or near the dissolution front. Since the front moves within the domain, this would require the use of fine gridblocks everywhere where the front is expected. This may require the use of rather fine grids for the entire domain, with the result that computational performances would become very poor. One elegant way of bypassing this drawback would be the introduction of Adaptive Mesh Refinement with refinement criteria triggered by the dissolution front and boundary layer characteristic lengths, i.e., porosity and concentration gradients. We discuss the implementation of such an AMR algorithm in the next section, based on a finite volume discretization of the involved PDEs.

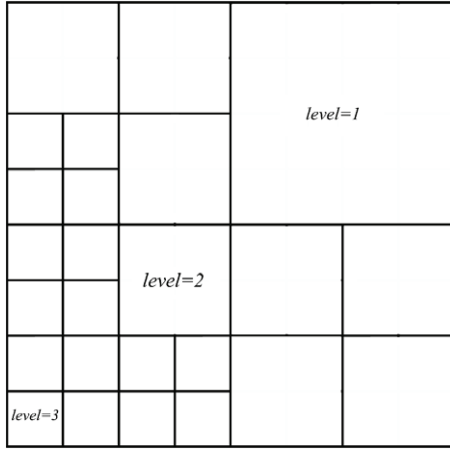


Fig. 1. An example of an AMR grid with 3 levels.

4. Adaptive mesh refinement

The AMR grid system (see Fig. 1) is based on a combination of Cartesian grid blocks under different levels from the coarsest grid level (named level = 1) to the finest grid level (named level = l_{max}). Only part of the grid blocks in a certain level will be activated according to a user-defined refinement criterion, and the set of active grid blocks from all the levels make a compact cover of the whole computational domain. For numerical convenience, the maximum level number, l_{max} , is also a user-defined value, which can easily be modified and may be adapted to a requested accuracy and computational efficiency. In order to have a simpler interface topology, we adopt a 2:1 ratio for the mesh sizes between two adjacent grid levels. The ratio 2:1 is chosen also because it allows for fast indexing and searching, and it leads to more straightforward integration schemes across the fine/coarse boundaries, while higher ratios may lead to reductions in accuracy. Different grid levels will be solved simultaneously with an identical time step. At each time step, we solve the whole domain fully implicitly and then perform the regriding according to the refinement criteria.

4.1. A fully implicit scheme to solve the PDE equations

We solve the problem in the whole computational domain for all the active-cell variables. Special care must be taken to the coupling at interfaces between gridblocks of different levels. In the following, we present the finite volume scheme used for the equation discretization in the two dimensional case. This scheme can be easily extended to three-dimensional cases. The Newton–Raphson method is used for solving the resulting non-linear equations.

Eq. (8) is an ODE and we solve it using a simple Euler implicit scheme

$$[\rho_s \varepsilon_l]_{i,j}^{t+\Delta t} - [\rho_s \varepsilon_l]_{i,j}^t = \Delta t [\rho_l \alpha (\Omega_{eq} - \Omega_{Al})]_{i,j}^{t+\Delta t} \quad (15)$$

where the subscript i, j refers to the actual gridblock. Higher order ODE solvers can be used if necessary, but the coupling between porosity and concentration in the above equation limits the possibilities. The solid density ρ_s may be variable in general but in our cases we consider it as a constant.

The discretization of Eq. (9) will be performed with Eq. (13) altogether. In the scope of the AMR grid, one particular issue is the calculation of fluid velocity fluxes across the interfaces between the grid blocks of different levels, such as the pattern illustrated in Fig. 2. A traditional approach was to directly calculate the pressure difference using the cell-centered pressure values or to apply

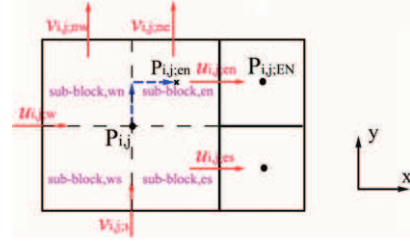


Fig. 2. Scheme for the calculation of the velocity flux at the grid block interface for adjacent levels.

interpolation formulas to obtain the values on the interfaces [41]. However, it has been recognized that such methods lead to inaccurate fluxes, which can be increased by different factors like, for instance, the heterogeneity of the transport properties, unstable flows induced by gravity forces, the connecting line of the two center points being far away from the center of the interface. To overcome the limitation, we propose a special scheme to compute the flux at the interfaces, which can be found in the Appendix.

The velocity is then substituted into the total liquid mass balance equation (9). Its discretized form can be finally expressed as follows

$$\begin{aligned} & \{[\varepsilon_l \rho_l]_{i,j}^{t+\Delta t} - [\varepsilon_l \rho_l]_{i,j}^t\} \Delta x_{i,j} \Delta y_{i,j} \\ & + [(\rho_l u_l)_{i,j;e}^{t+\Delta t} - (\rho_l u_l)_{i,j;w}^{t+\Delta t}] \Delta t \Delta y_{i,j} \\ & + [(\rho_l v_l)_{i,j;n}^{t+\Delta t} - (\rho_l v_l)_{i,j;s}^{t+\Delta t}] \Delta t \Delta x_{i,j} \\ & = [\rho_l \alpha (\Omega_{eq} - \Omega_{Al})]_{i,j}^{t+\Delta t} \Delta t \Delta x_{i,j} \Delta y_{i,j} \end{aligned} \quad (16)$$

where the liquid density ρ_l varies with time because it is a function of concentration. In Eq. (16), if there are two neighbor grids at one side, say east, $(\rho_l u_l)_{i,j;e}^{t+\Delta t}$ is taken as the average of $(\rho_l u_l)_{i,j;es}^{t+\Delta t}$ and $(\rho_l u_l)_{i,j;en}^{t+\Delta t}$.

For the discretization of the mass balance equation of species A, Eq. (10), we use a second-order scheme for the diffusion term and an upstream weighting scheme for the convection term. Since these schemes are rather classical, we do not give many mathematical details. Accordingly, we discretize Eq. (10) as:

$$\begin{aligned} & \{[\varepsilon_l \rho_l \Omega_{Al}]_{i,j}^{t+\Delta t} - [\varepsilon_l \rho_l \Omega_{Al}]_{i,j}^t\} \Delta x_{i,j} \Delta y_{i,j} \\ & + [\rho_l u_l]_{ups}^{t+\Delta t} \cdot [(\Omega_{Al})_{i,j;e} - (\Omega_{Al})_{i,j;w}]^{t+\Delta t} \Delta t \Delta y_{i,j} \\ & + [\rho_l v_l]_{ups}^{t+\Delta t} \cdot [(\Omega_{Al})_{i,j;n} - (\Omega_{Al})_{i,j;s}]^{t+\Delta t} \Delta t \Delta x_{i,j} \\ & = 2 \Delta t \Delta x_{i,j} \Delta y_{i,j} \left\{ (\varepsilon_l \rho_l D_{Al}^*)_{i,j;e} \frac{[(\Omega_{Al})_{i,j;E} - (\Omega_{Al})_{i,j}]}{\Delta x_{i,j} + \Delta x_e} \right. \\ & \quad \left. - (\varepsilon_l \rho_l D_{Al}^*)_{i,j;w} \frac{[(\Omega_{Al})_{i,j} - (\Omega_{Al})_{i,j;W}]}{\Delta x_{i,j} + \Delta x_e} \right\}^{t+\Delta t} \\ & + 2 \Delta t \Delta x_{i,j} \Delta y_{i,j} \left\{ (\varepsilon_l \rho_l D_{Al}^*)_{i,j;n} \frac{[(\Omega_{Al})_{i,j;N} - (\Omega_{Al})_{i,j}]}{\Delta y_{i,j} + \Delta y_n} \right. \\ & \quad \left. - (\varepsilon_l \rho_l D_{Al}^*)_{i,j;s} \frac{[(\Omega_{Al})_{i,j} - (\Omega_{Al})_{i,j;S}]}{\Delta y_{i,j} + \Delta y_s} \right\}^{t+\Delta t} \\ & + \Delta t \Delta x_{i,j} \Delta y_{i,j} [\rho_l \alpha (1 - \Omega_{Al}) (\Omega_{eq} - \Omega_{Al})]_{i,j}^{t+\Delta t}. \end{aligned} \quad (17)$$

In Eq. (17), the properties, e.g., $\varepsilon_l \rho_l D_{Al}^*$, on the interfaces are calculated by harmonic averages of the point values on both sides. The upstream weighting expressions are obtained from the

upstream direction, for example,

$$[\rho_l u_l]_{ups}^{t+\Delta t} \cdot [(\Omega_{Al})_{i,j;e} - (\Omega_{Al})_{i,j;w}]^{t+\Delta t} = \begin{cases} [\rho_l u_l]_{i,j;w}^{t+\Delta t} \cdot [(\Omega_{Al})_{i,j} - (\Omega_{Al})_{i,j;W}]^{t+\Delta t} & \text{if } ([u_l]_{i,j;w} + [u_l]_{i,j;e}) \geq 0 \\ [\rho_l u_l]_{i,j;e}^{t+\Delta t} \cdot [(\Omega_{Al})_{i,j;E} - (\Omega_{Al})_{i,j}]^{t+\Delta t} & \text{if } ([u_l]_{i,j;w} + [u_l]_{i,j;e}) < 0. \end{cases} \quad (18)$$

In Eqs. (17) and (18), if there are two neighboring grid blocks at one side, say east, the quantities with subscript e , e.g., $[\psi]_{i,j;e}$, $[\psi]_{i,j;E}$, are taken as the average of $[\psi]_{i,j;es}$ and $[\psi]_{i,j;en}$, and the average of $[\psi]_{i,j;ES}$ and $[\psi]_{i,j;EN}$, respectively. We are able to make this simplification because the variation of the quantities in a coarse grid block is small, as controlled by the refinement criteria.

Eq. (15) through Eq. (18) are solved in a fully implicit manner using the Newton–Raphson algorithm.

4.2. Regridding

Since the dissolution front is moving, the grid structure may need to be updated with time to maintain a given accuracy. Therefore, regridding should be performed at each time step according to given refinement criteria. There are several types of refinement criteria. Some AMR methods use Richardson extrapolation [34] to estimate the local truncation errors and determine where the solution accuracy is insufficient. It may produce larger refined regions than desired for some applications. Another popular way is based on the values of the gradient of the physical variables of interest [50]. Similar to the latter approach but simpler to implement, we propose to use refinement criteria based on the variations of the physical quantities, var_{ε_l} , $var_{\Omega_{Al}}$, within a coarse block, such as

$$var_{\varepsilon_l} = \max\{\varepsilon_l\}_C - \min\{\varepsilon_l\}_C \quad \forall C \in \hat{C}_{i,j;lev} \quad (19)$$

$$var_{\Omega_{Al}} = \max\{\Omega_{Al}\}_C - \min\{\Omega_{Al}\}_C \quad \forall C \in \hat{C}_{i,j;lev} \quad (20)$$

in which $\{\varepsilon_l\}_C$ and $\{\Omega_{Al}\}_C$ are the interpolated values of the finest gridblocks, interpolated from the values of the active coarse blocks (coarser than the finest grid blocks) using a bi-linear interpolation approach [39], which is simple and fast. $\hat{C}_{i,j;lev}$ represents the extended domain (marked with a blue rectangular frame in Fig. 3) that includes $C_{i,j;lev}$ (the domain of a coarse grid block which is located at i, j at refinement level = lev and marked with a red rectangular frame in Fig. 3) and its neighboring finest cells. In the formula above, “ max ” refers to the maximum value and “ min ” refers to the minimum value in the relevant domain.

In order to decide about the next used AMR grid, the entire domain is first scanned for all the coarse blocks. The variations (Eqs. (19) and (20)) are calculated and, if the variations var_{ε_l} and $var_{\Omega_{Al}}$ in the extended domain of a coarse grid block, e.g., $\hat{C}_{i,j}$, are less than the refinement criteria values, then we can consider that the physical quantities in this coarse grid are smooth enough so that this coarse gridblock is marked as active. Otherwise, it will be marked as inactive. Based on our practice, the refinement criteria can be chosen as $var_{\varepsilon_l} \leq 0.05$ and $var_{\Omega_{Al}} \leq 0.1\Omega_{eq}$. If all the coarse gridblocks are marked as active, then the AMR grid remains for the next time step. Otherwise, any inactive block will trigger the generation of new AMR grid. Generating the new AMR grid starts from the coarsest level to the finest one by marking the gridblocks as active or inactive based on the refinement criteria. In this manner, the originally coarse gridblocks could be refined and the originally fine gridblocks could be coarsened. It is mentioned that when generating the AMR grid, an additional requirement has to be considered: the level difference between adjacent gridblocks

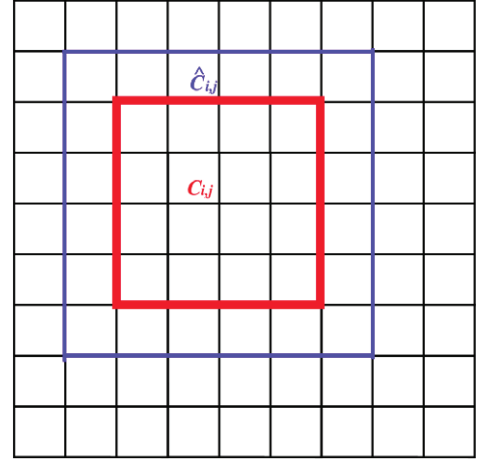


Fig. 3. A coarse grid block $C_{i,j}$ and its extended region $\hat{C}_{i,j}$. (For interpretation of the references to colour in this figure legend, the reader is referred to the web version of this article.)

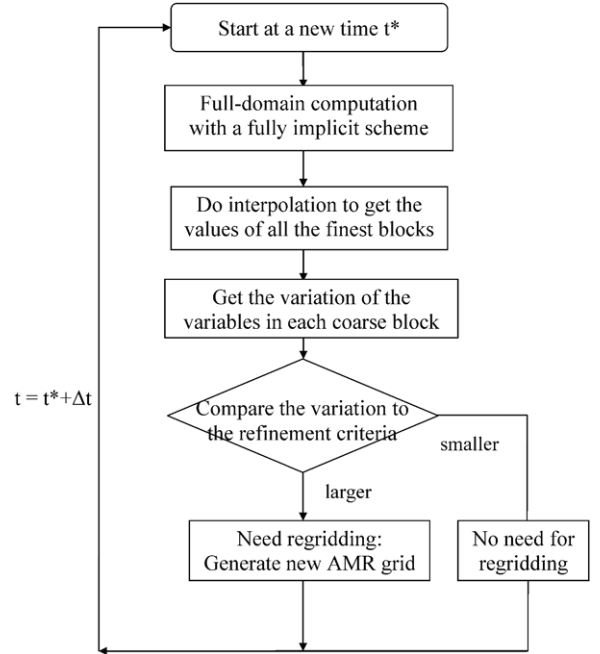


Fig. 4. Flowchart of the proposed AMR procedure.

cannot be greater than 1 in order to avoid a strong contrast between adjacent mesh sizes.

The flowchart of the whole AMR procedure is shown in Fig. 4. We mention that the values of the finest blocks from interpolation are only used for regridding based on the refinement criteria. These values will not be assigned to the active blocks unless the blocks have changed in level.

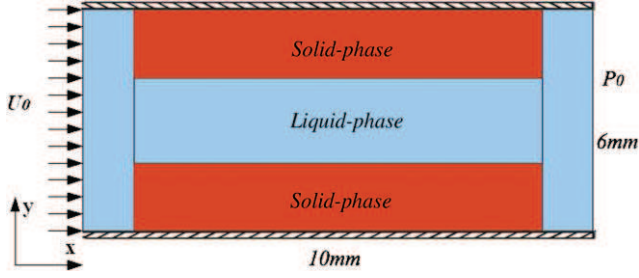
5. Simulation examples

Salt rock or Halite (NaCl) will be used as the dissolving species for the simulation examples presented in this section. The salt properties (NaCl) are given in Table 1. We carried out three numerical examples. The first 2D example is used to validate our own code implementation by convergence studies and comparing to the results obtained with a Comsol Multiphysics® implementation. We would like to mention that the DIM model was validated in [31] against the ALE solutions (sharp-front model) for dissolution problems, so that we will not repeat it

Table 1

The rock salt properties used for the simulation examples.

Parameter	Value	Unit
ρ_s	2.165×10^3	kg/m ³
ρ_l	$1.0 \times 10^3(1 + 0.7385\Omega_{Al})$	kg/m ³
μ_l	1.2×10^{-3}	kg/ms
D_{salt}	1.3×10^{-9}	m ² /s
α_L	0.01	m
Ω_{eq}	0.27	-

**Fig. 5.** The 2D geometry used for the simulation example. Salt blocks constitute the solid phase, water the liquid phase. The inlet (fluid velocity) is located at the left of the domain and the outlet at the right.

in this paper. The second example corresponds to the dissolution starting from a three-dimensional cylinder located in a salt block. The last example corresponds to the dissolution of a salt deposit, with fresh water vertically injected from the top (inlet).

5.1. 2D simulation

The purpose of this subsection is to validate our own code by comparing with the simulation results obtained by using Comsol Multiphysics[®]. In Comsol Multiphysics[®], we use Diffusion equation for Eq. (8) while setting the diffusion coefficient as 0, and use Darcy's Law (transient analysis) for Eq. (9), and use Convection-Diffusion equation for Eq. (10). The two-dimensional geometry used for the simulations is represented in Fig. 5. This example has two salt blocks (solid phase) with a length of 7 mm and a width of 2 mm placed symmetrically in a channel. The channel is 10 mm long and 6 mm wide and both lateral sides are impervious walls. In Comsol Multiphysics[®], the whole domain is separated into 5 subdomains (Fig. 5). These subdomains are identified as solid-phase subdomains and liquid-phase subdomains, which stand for salt blocks and water, respectively. Initial ε_l and Ω_{Al} are set as 0.01 and Ω_{eq} for the salt blocks, and 1 and 0 for the water, respectively. Rather than that, no explicit assignment of the solid-liquid interface is required because of the implicit interface feature of the DIM model. The Fresh water is injected from the left side to dissolve the salt blocks and the right boundary is at constant pressure (P_0). Gravity is neglected. Two flow conditions are considered: the advection dominated condition and the diffusion dominated condition. The first one is with a constant velocity $U_0 = 1.0 \times 10^{-5}$ m/s and the second one is with a constant velocity $U_0 = 1.0 \times 10^{-7}$ m/s. The referenced Péclet (Pe) numbers are calculated as $Pe = U_0 L / D_{salt}$ equaling to 20 and 0.2 for each case, where L is the width of the center channel. Because there is no real porous medium in the model, we use the width of the channel as the characteristic length l_c to calculate the permeability.

To do the validation, we perform the computations using 4 methods: Comsol Multiphysics[®], our own code using the uniformly fine grid, our own code using the proposed AMR scheme, and our own code using the traditional AMR scheme presented in [41]. Fig. 6 plots the mass fraction fields Ω_{Al} and the velocity

vectors \mathbf{V} on a 200×120 based grid, using the 4 methods under $Pe = 20$ and $Pe = 0.2$ for a time (2000 s) that shows clearly the dissolution profiles. Apparently, larger Pe leads to a faster dissolution, generating a gradual concentration distribution across the interfaces. The AMR method smartly tracks the interface using the finest gridblocks, while using coarser gridblocks elsewhere.

The computational solutions match well in a brief view using the first three methods, except that using the last method an inflection of the velocity vectors is observed around the regions where the fine and coarse cells are in connection. Fig. 7 plots the velocity along y -direction (V_y) at the central cross section at $Pe = 20$ and $Pe = 0.2$. One sees that using a traditional AMR scheme leads to fluctuation of velocity, while using the proposed AMR scheme gives very close solutions compared to Comsol Multiphysics[®].

Further, we show in Fig. 8 the L^2 relative difference of the solutions between Comsol Multiphysics[®] and our own code computed on the same uniform grid (200×120) under different Pe numbers. The relative difference of the solution is defined by

$$\epsilon = \frac{\int_V (\psi_{comsol} - \psi_{owncode})^2 dV}{\int_V (\psi_{comsol})^2 dV} \quad (21)$$

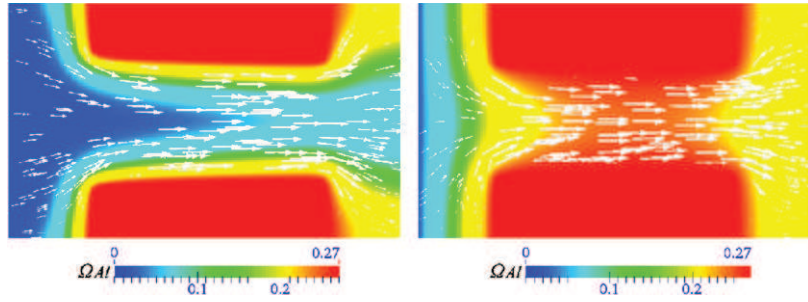
in which ψ_{comsol} represents the solution obtained by Comsol Multiphysics[®], $\psi_{owncode}$ represents the solution obtained by our own code, and V is the volume of the domain. It is observed that the relative differences of both the mass fraction Ω_{Al} and the magnitude of the velocity \mathbf{V} are below 0.01 for all the space steps, showing a good agreement between the two solvers. The reason that the relative differences do not change much with the space steps should come from the intrinsic difference between the FEM solver (Comsol Multiphysics[®]) and the FVM solver (our own code).

Grid convergence studies are performed for Comsol Multiphysics[®] and our own code, respectively, which are shown in Fig. 9. The L^2 relative error is calculated using the following form:

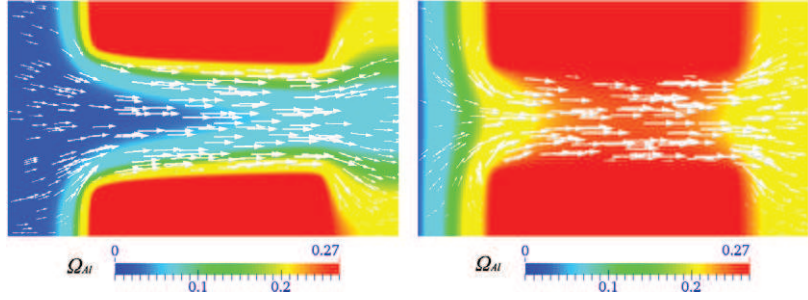
$$relativeerror = \frac{\int_V (\psi_{(\Delta t, \Delta x)} - \psi_{ref})^2 dV}{\int_V (\psi_{ref})^2 dV} \quad (22)$$

in which $\psi_{(\Delta t, \Delta x)}$ represents the solution using an exact temporal step and spatial step, and ψ_{ref} represents the solution using very small time step and space step (because the spatial steps are different, ψ_{ref} is the average of the referenced solution over the volume of the grid block corresponding to $\psi_{(\Delta t, \Delta x)}$). The convergence study shows that for both Comsol Multiphysics[®] and our own code, there are approximately a first order accuracy for the mass fraction Ω_{Al} and the magnitude of the velocity \mathbf{V} in time under both Pe conditions. When Pe is large ($Pe = 20$), there are approximately a first order accuracy for Ω_{Al} and a second order accuracy for the magnitude of \mathbf{V} in space. When Pe is small ($Pe = 0.2$), the order of accuracy is approximately 1.5 for Ω_{Al} and approximately 1.7 for the magnitude of \mathbf{V} in space. These convergence rates are in accordance with the orders of the numerical scheme we use in which the diffusion term has a second order accuracy and the advection term has a first order accuracy. We also notice that the temporal relative errors are much smaller than the spatial relative errors, i.e., numerical errors from the spatial discretization are dominating in this case.

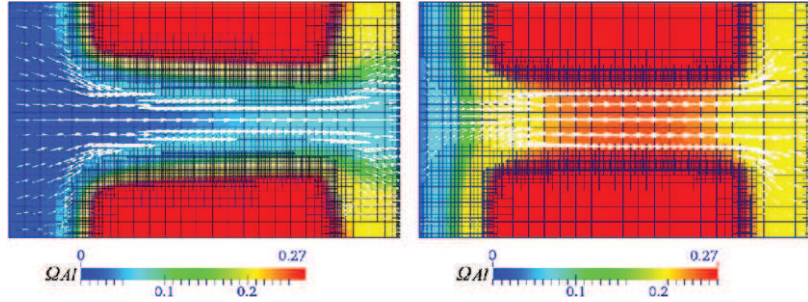
The grid convergence studies are then carried out for the AMR methods. Using the solutions from our own code with very small uniform spatial steps as the reference, we show in Fig. 10 the L^2 -norm relative errors using the proposed AMR method in this paper and the traditional AMR method presented in [41]. For the proposed AMR method, it shows that the order of accuracy is approximately 0.9 for the mass fraction Ω_{Al} , and is approximately 1.7 for the magnitude of the velocity \mathbf{V} , which



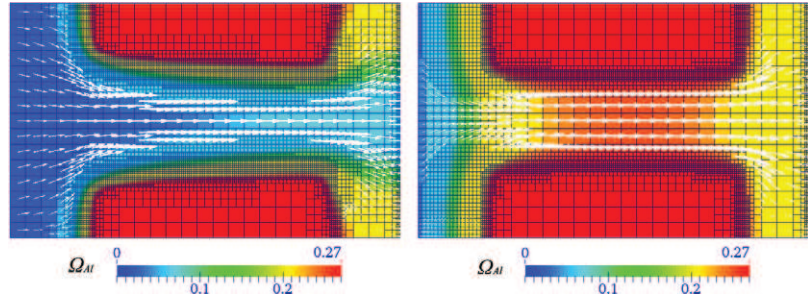
(a) Consol Multiphysics[®] solutions (Left: $Pe = 20$; Right: $Pe = 0.2$).



(b) Own code solutions using uniformly fine grid (Left: $Pe = 20$; Right: $Pe = 0.2$).



(c) Own code solutions using the proposed AMR scheme (Left: $Pe = 20$; Right: $Pe = 0.2$).



(d) Own code solutions using the traditional AMR scheme by Forsyth and Sammon [41] (Left: $Pe = 20$; Right: $Pe = 0.2$).

Fig. 6. Plots of Ω_{Al} and velocity vectors \mathbf{V} at time $t = 2000$ s under different Pe numbers using 4 different methods.

is a good accuracy. However, for the latter AMR method, the order of accuracy is approximately 0.7 for the mass fraction Ω_{Al} , and is approximately 0.5 for the magnitude of the velocity \mathbf{V} , showing unsatisfying accuracies, especially for the velocity. This is in accordance with our previous comment on this traditional AMR method. Therefore, the AMR method proposed in this paper shows a better performance compared with a traditional AMR method for the DIM dissolution case. Besides that, all these studies have served as validation test cases for our own code (note that several other comparisons have been performed in order to check our own code).

5.2. 3D core-scale simulation

In this example, we simulate the dissolution of a three-dimensional salt block as sketched in Fig. 11. A salt block is placed in the center of a box (dimensions: 20 mm long, 10 mm wide, and 10 mm high). A cylindrical hole is drilled in the center of the salt block with a radius of 2 mm, thus allowing the fluid to go through. Pure water is injected into the box from the right boundary with a constant velocity $U_0 = 10^{-5}$ m/s. Water dissolves the salt solid and the salt solution (brine) leaves the domain from the left boundary. The other sides have no-flow boundary conditions.

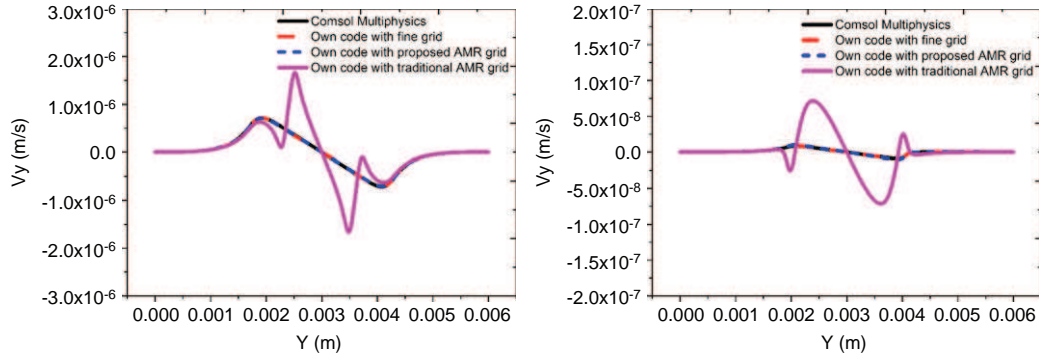


Fig. 7. Y-direction velocity at the central cross section for the 4 methods under $Pe = 20$ and $Pe = 0.2$.

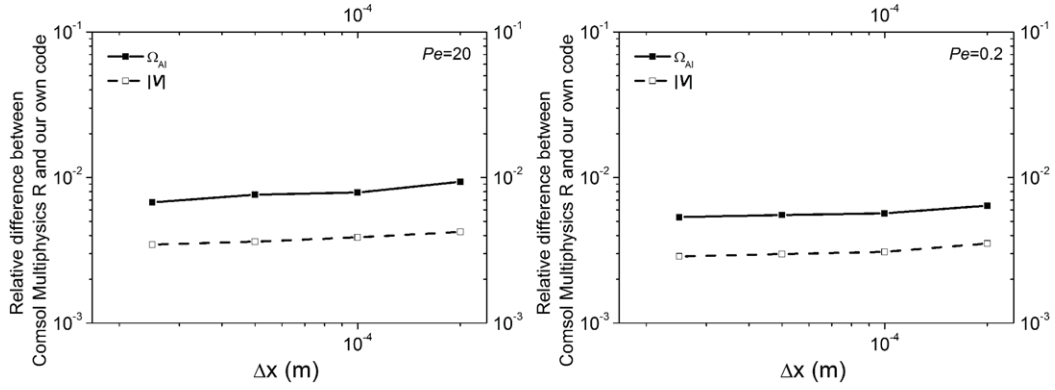


Fig. 8. Relative difference of the solutions between Comsol Multiphysics[®] and our own code on the uniform grids under $Pe = 20$ and $Pe = 0.2$.

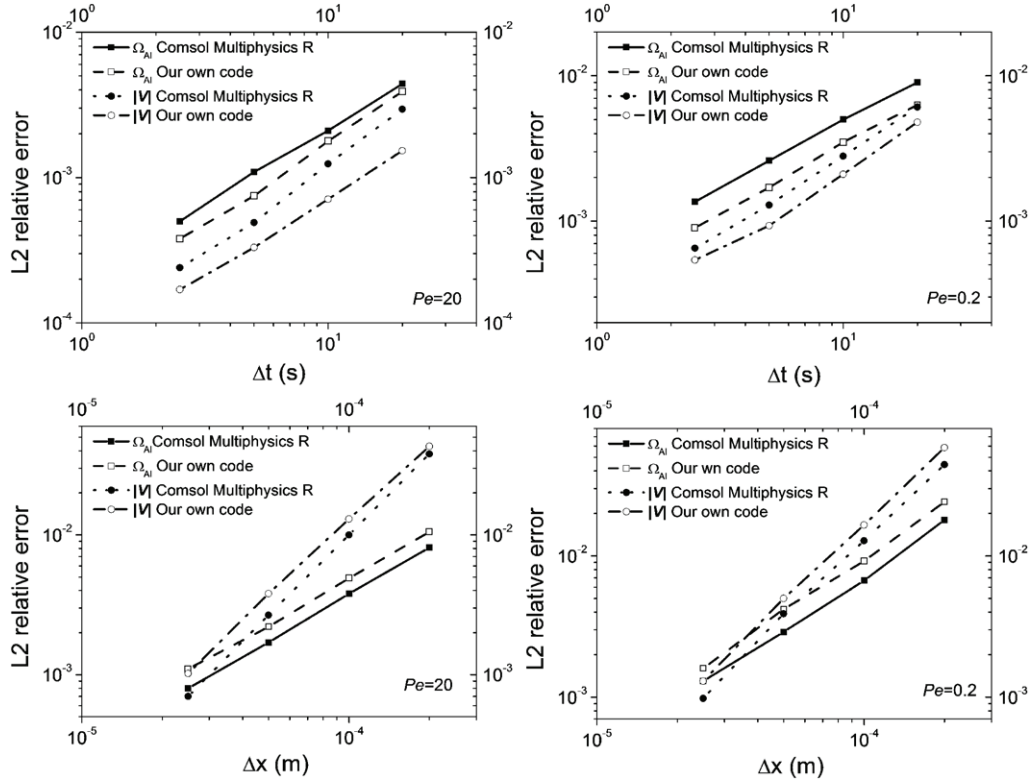


Fig. 9. Temporal and spatial L^2 -norm relative errors of the solutions using Comsol Multiphysics[®] and our own code under $Pe = 20$ and $Pe = 0.2$.

Gravity is in the y -direction. While convective instabilities may arise in the true physical system if density variations are taken into account and break the symmetry of the geometry, we will only

solve over the half part of the domain, whose axial surface is the central x - y plane, for our numerical tests purposes. Conditions of symmetry are imposed on this boundary. The Pe number is about

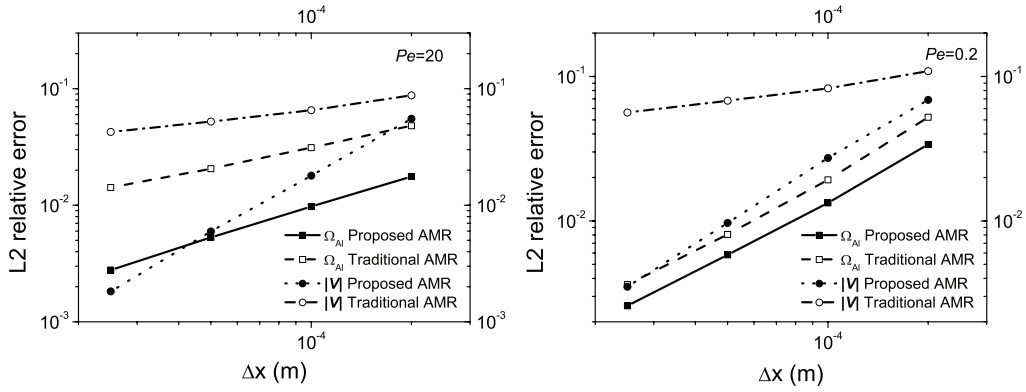


Fig. 10. Spatial L^2 -norm relative errors of the solutions using the proposed AMR and the traditional AMR scheme under $Pe = 20$ and $Pe = 0.2$.

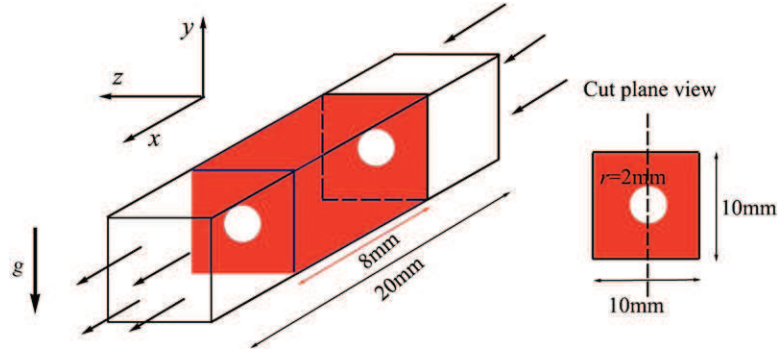


Fig. 11. Example of a 3D salt block dissolution with a cylindrical hole in the center.

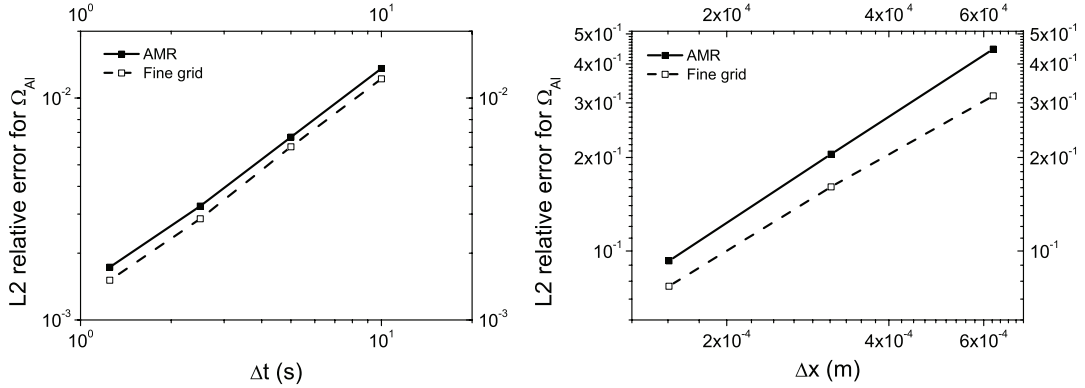


Fig. 12. Temporal and spatial relative errors of the mass fraction Ω_{Ai} for the 3D example using the AMR and fine grid.

40, and the Rayleigh number Ra , where $Ra = \frac{\Delta \rho l_{max} g |K_{max} d}{\mu_l D_l}$ and d is the diameter of the hole, is about 300 in this case.

We first perform a convergence study for the time steps and the space steps using the AMR and the fine grid. We compute the example using $32 \times 16 \times 8$, $64 \times 32 \times 16$, and $128 \times 64 \times 32$ based grids with a variation of time steps from 1 to 10 s. Because the three-dimensional computations are extremely expensive with respect to both the time and memory resources, it is difficult to obtain the solutions using a very fine grid size with common desktop computers (this was not the purpose of this study to port the calculations to special computing facilities). Therefore, we use Richardson extrapolation to approximate the referenced solutions which are used in calculating the relative errors (we are aware that this extrapolation method is not perfect but it is usable when there is a convergence trend). The L^2 -norm relative errors of the mass fraction Ω_{Ai} are plotted in Fig. 12. It shows that the temporal relative errors have a first-order accuracy and are much smaller than the spatial relative errors. The order of the accuracy for space

is approximately 1.2. The spatial relative errors are large using the $32 \times 16 \times 8$, $64 \times 32 \times 16$ grid, and it is about 0.09 using the $128 \times 64 \times 32$ based grid for the AMR. Even though the error is still not small enough, we use it as a reference for plotting the computational results to avoid excessive computational time and memory resources.

We therefore plot the computational results using the $128 \times 64 \times 32$ based grid, and the AMR grid structure is built with this fine mesh as the finest level. The maximum time step is set as 10 s. We are able to estimate the Courant number, $C = \frac{u_{max} \Delta t}{\Delta x}$, to be 5.3. Such a value of the Courant number much greater than 1 indicates the advantage of using the implicit scheme with cell-based methods. For the AMR computations, we set the total level number equal to 5 and the refinement criteria to $var_{\epsilon_l} = 0.05$ and $var_{\Omega_{Ai}} = 0.1 \Omega_{eq}$. The time evolution of the salt mass fraction Ω_{Ai} from 1000 to 5000 s is presented in Fig. 13. The left side is for AMR result and the right side is for the fine-grid solution. Since gravity is taken into account, natural convection

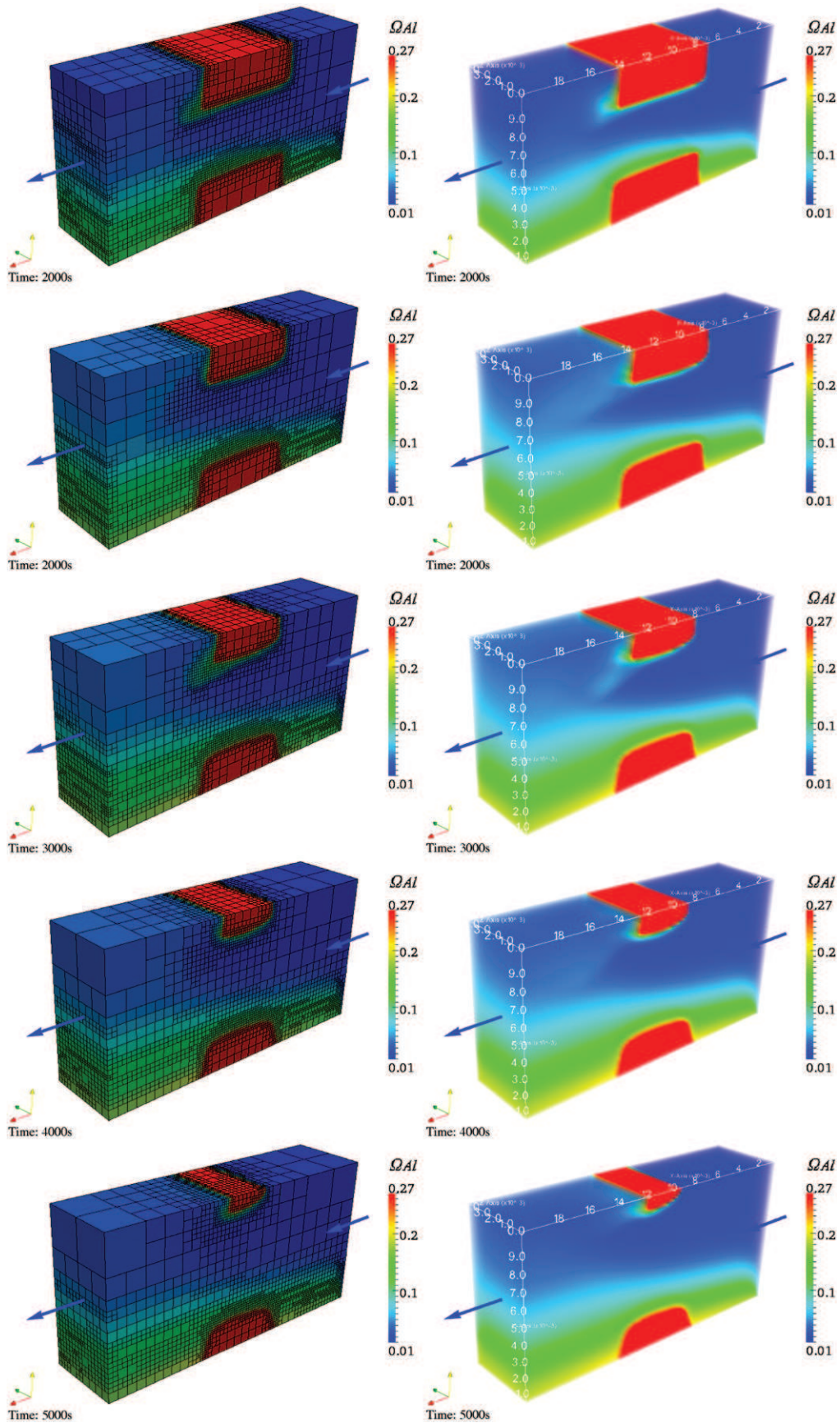


Fig. 13. Time evolution of the salt mass fraction Ω_{Al} using the AMR method (left) and fine-grid solution (right). From 1000 to 5000 s, salt block is getting smaller and smaller due to dissolution. The finest mesh is moving with the solid-liquid interface for the AMR method, showing better computational efficiency. Caused by natural convection, salt plumes fluctuating with time can be found at the tail of the salt block.

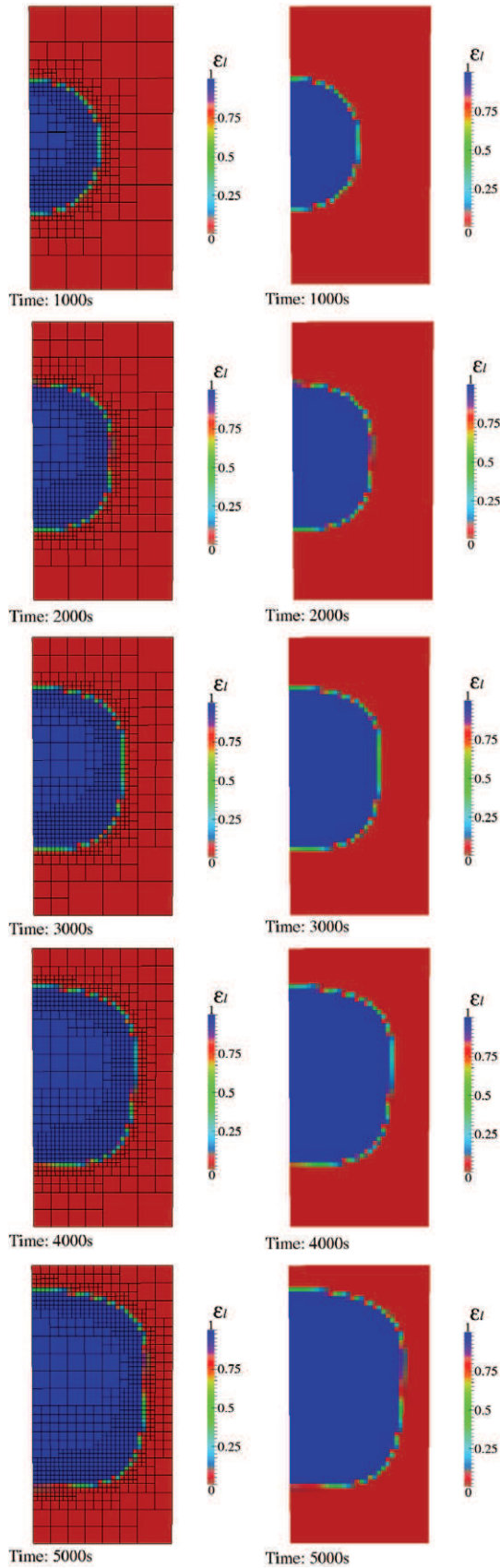


Fig. 14. Time evolution of the porosity ε_l at the central cross-section using the AMR method (left) and fine-grid resolution (right).

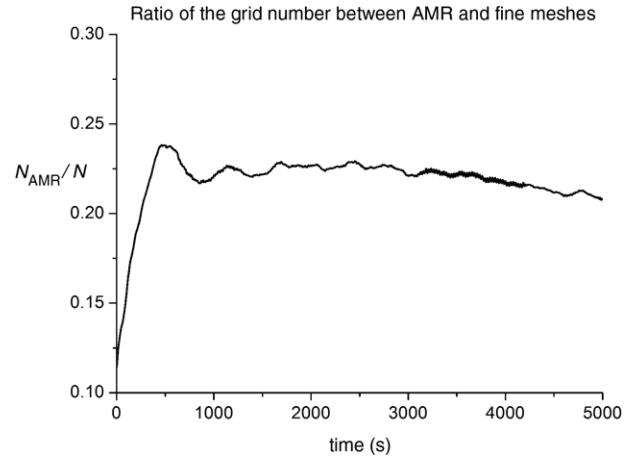


Fig. 15. The ratio of the grid block numbers between AMR and fine-grid resolutions.

induced by the fluid density gradient can be observed with a fluctuating concentration plume near the downstream and upper side of the salt block. These numerical results illustrate the ability of the proposed AMR algorithm to follow such hydrodynamics instabilities as it also refines the grids where the gradient of the mass fraction Ω_{Al} is large. In Fig. 14, we plot the time evolution of the porosity ε_l in the cross central section (perpendicular to the x -axis). The computations show that the round-shape tube cross-section expands with time, and that the upper side is dissolving faster than the side below due to gravity segregation (concentration is higher at the bottom or concentration gradient is lower, leading to a lower dissolving power). The simulation results agree very well between the AMR and the uniformly fine grid.

For the computational part, the linear matrix system is solved by an efficient solver PARDISO [51]. The CPU times are 2.2 h and 43.5 h with AMR and uniform fine grids, respectively (using a single computer with an Intel i5-2320 CPU and 16 Gb RAM). The CPU time reduction ratio with the AMR method is about 20 times, which is very attractive. Of course, using other solvers may change the ratio. Nevertheless, technical discussions for the competition of solvers would not be carried out in this paper. Fig. 15 plots the time evolution of the grid block number ratio between the AMR and uniform fine grids, showing that the reduction of gridblocks is pronounced using the AMR. It also shows that the AMR grid block number increases at the beginning as the salt mass is transported into the liquid, and then it decreases after a certain time since the volume of the salt block shrinks, indicating the flexibility and efficiency of the AMR method tracking the dissolution fronts.

Fig. 13 shows a certain degree of natural convection with fluctuating salt plumes which mainly happens at the tail of the salt block interfaces. To some extent, this physical instability is not as strong as those observed in [31] using a horizontal fracture with infinite upper and lower planes (which can be simplified as a 2D horizontal fracture). For comparison purposes, we performed a 2D simulation case (simplified from 3D infinite fracture) whose geometry is the projection of Fig. 11 to the x - y plane with the same other conditions as in the 3D tube case. The salt mass fraction, Ω_{Al} , at time 100 and 1000 s, is shown in Fig. 16. At early times, i.e., at $t = 100$ s in the figure, strong density variations are developing from the dissolving interfaces, which trigger the development of a number of dissolution fingers initializing from the top salt wall where the situation is unstable. At 1000 s, the mass boundary layers are thicker, hence less prone to salt fingering. At the same time, convection tends to flush the salt plumes toward the right domain outlet. Further, we extended the length of the salt block from 8 to 16 mm and performed another simulation to observe the impact of the length/width ratio of the fracture on fingering.

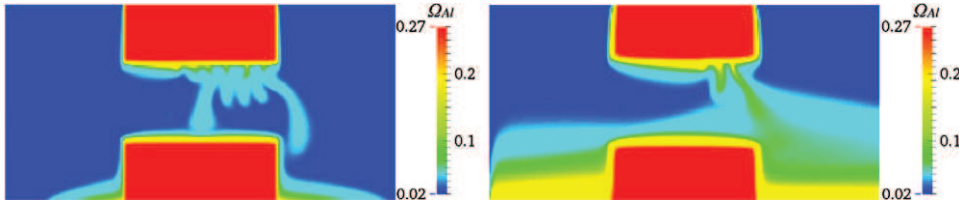


Fig. 16. Ω_{Ai} for a 2D simulation with gravity at time 100 and 1000 s.

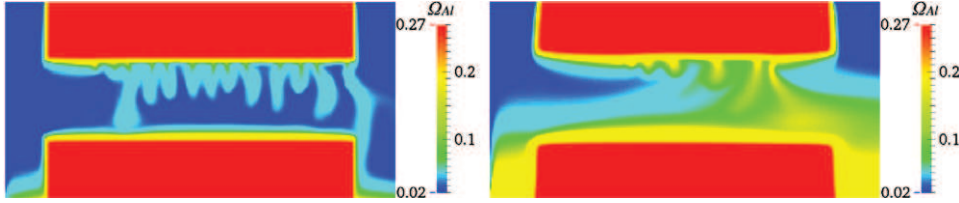


Fig. 17. Ω_{Ai} for a 2D simulation with gravity with longer salt blocks at time 100 and 1000 s.

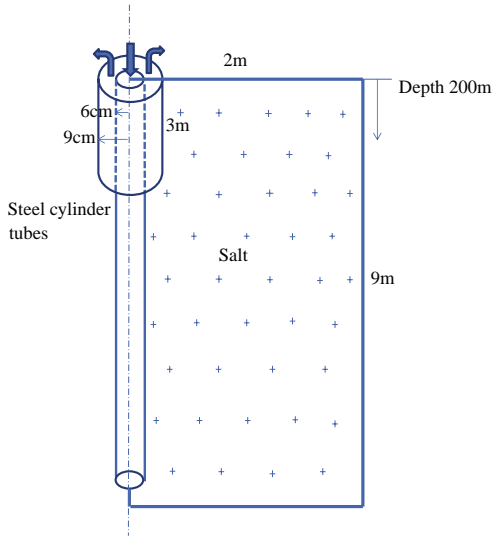


Fig. 18. Example of 2D-axisymmetrical dissolution using a vertical centered double-well, with vertical (inner tube) injection-inlet and production-outlet (outer tube).

Fig. 17 shows that there are more salt plumes in the flow domain, which is similar to the patterns observed in [31]. The differences between the horizontal fracture and tube behaviors are not due to numerical problems but are rather attached to physical and topological considerations. In the horizontal fracture case, a flat boundary layer with destabilizing buoyancy effects develops at

the top wall. Hydrodynamic instabilities will develop after some critical Rayleigh number is reached. On the contrary, in the 3D tube case, the existence of “lateral” walls “parallel” to gravity will trigger natural convection as soon as diffusion starts, with the dense fluid going down from the top *along* the lateral walls. A much larger Rayleigh number must be reached in order to get true salt fingering superposed to these more gentle convective patterns. Therefore, this study shows that a horizontal fracture with two upper and lower dissolving planes will generate stronger gravity-driven physical instabilities, i.e., salt fingering, than the 3D horizontal tube configuration. As far as we know, this finding was not mentioned in the literature because most references were focused on fractures with two horizontal sides, such as Dijk and Berkowitz [52]; Dijk et al. [53]. They also showed that there is an enhancement of dissolution due to buoyancy patterns at the upper wall as compared to the lower part corresponding to a stable boundary layer, which is consistent with our findings and the results published in [31]. If boundary layers are not perpendicular to gravity, convective cells start earlier as illustrated in our study or in the study of dissolution in a vertical fracture by Oltéan et al. [16].

5.3. Reservoir-scale simulation

In this subsection, we attempt to have a preliminary study for large-scale dissolution problems using the DIM method combined with the AMR methods. We simulate a reservoir-scale dissolution problem: typically, the dissolution of a salt deposit from a well injection, as shown in Fig. 18. The well cavity dissolution device is described by an inner tube and an outer tube drilled into the

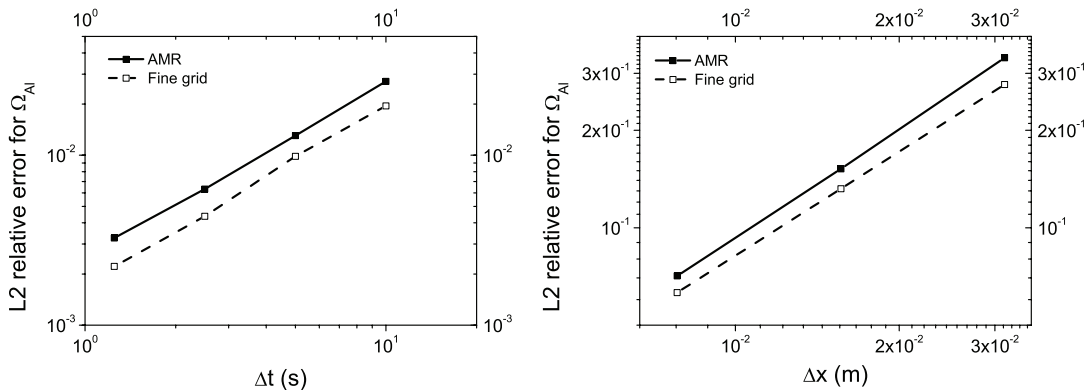


Fig. 19. Temporal and spatial relative errors of the mass fraction Ω_{Ai} for the reservoir-scale example using the AMR and fine grid.

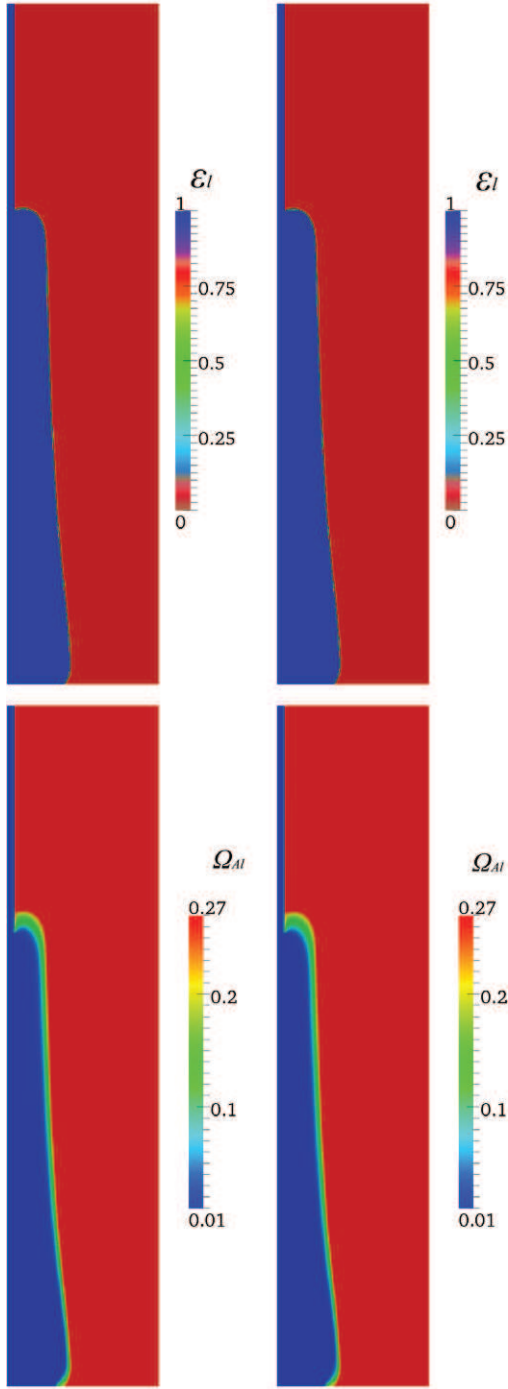


Fig. 20. Simulation results (ε_l and Ω_{Al}) using AMR method (left) and fine-grid solution (right) at time = 2 days.

center of the salt deposit. Pure water is injected vertically from the top into the inner tube with a constant velocity $U_0 = 0.02$ m/s and the salt solution is produced from the outer tube. The deposit is 9 m high with a radius of 2 m. The inner tube is 8.9 m long and has a radius of 0.06 m while the outer tube is 3 m long with a radius of 0.09 m. Water is injected from the top surface of the inner tube and is recovered from the top surface of the outer tube. Other boundaries are regarded as no-flow barriers. Since the deposit geometry is symmetric, this three-dimensional problem will be simplified into a two-dimensional axi-symmetric case, neglecting the potential of bifurcation phenomena breaking the axial symmetry.

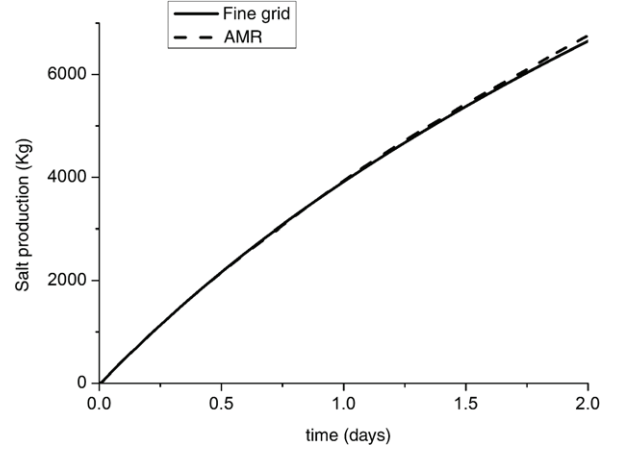


Fig. 21. Cumulative salt production for both AMR and fine grid.

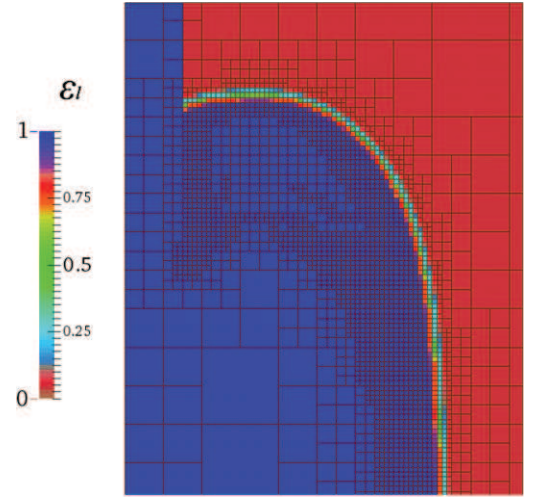


Fig. 22. An enlargement of ε_l and grid near the bottom side of outlet tube using AMR at time = 2 days.

We first perform a convergence study for both the time steps and the space steps. We compute the example using 1152×256 , 576×128 , and 288×64 based grids with a variation of time steps from 1 to 10 s. With the same reason as that for the previous example, we use Richardson extrapolation to approximate the referenced solutions to calculate the relative error. The L^2 -norm relative errors of mass fraction Ω_{Al} are plotted in Fig. 19. It shows that the temporal relative errors have a first-order accuracy and are much smaller than the spatial relative errors. The order of the accuracy for space is approximately 1.1. The spatial relative error is about 0.07 using the 1152×256 based grid for the AMR.

In this case, the 1152×256 based grid along the y -axis and r -axis with the time step to be 10 s is used for showing the computational results. The Courant number is estimated to be 25, which also shows the capability to compute under large Courant numbers using the fully implicit method with the cell-based AMR. The total grid level for the AMR computation is set to be 5 and the refinement criteria is set at $var_{\varepsilon_l} = 0.05$ and $var_{\Omega_{Al}} = 0.03$.

The simulation results at time = 2 days are plotted in Fig. 20 for ε_l (upper) and Ω_{Al} (below), respectively. The left side is for AMR results and the right side is for uniform fine grid computations. The interfaces are artificially diffused by the DIM model to several centimeters. This is an important contribution to the reservoir-scale simulations combined with the AMR method. We also show in Fig. 21 the outlet cumulative salt production. Both figures show

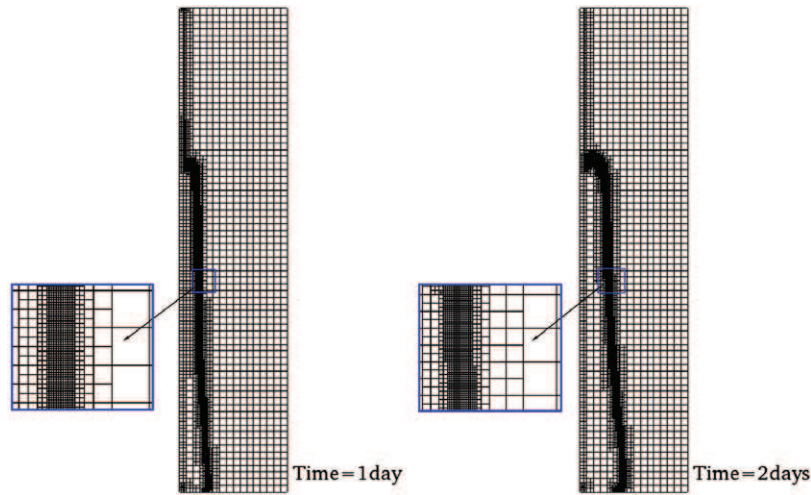


Fig. 23. AMR grid structures at time = 1 day and time = 2 days.

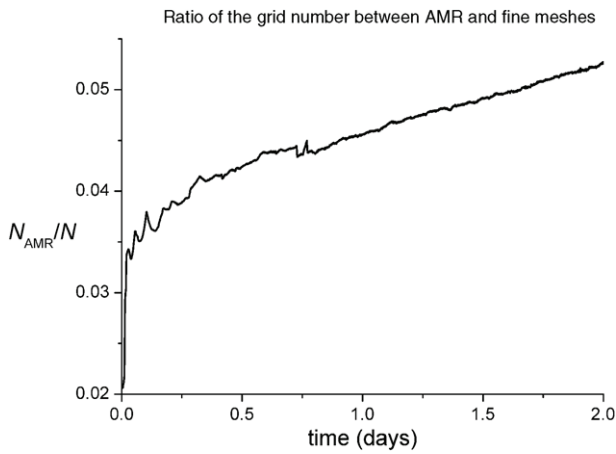


Fig. 24. The ratio of the grid block numbers between AMR and fine-grid resolutions.

that the simulation results match very well between the AMR and uniform fine grid resolutions. We can also observe that the developed method can easily handle geometrical singularities such as the ones related to the tubing. For example, we show in Fig. 22 an enlargement of ε_l and grid near the tubing outlet. Dissolution near this region is well described and calculations do not show any particular numerical problem, which might not be easily handled by the sharp-front methods, such as ALE.

During the rock salt dissolution, the interface keeps moving outward. We plot in Fig. 23 the AMR grid structures at $time = 1$ day and $time = 2$ days. This shows that the finest grid blocks are found only near the interface. In the other regions, like those deep inside the salt deposit and those far away from the interface in the liquid, the gridblocks are very coarse. This is the reason why the AMR algorithm can be so efficient. Indeed, the CPU times (same computer as before) were measured to be 1.6 and 49.2 h for AMR and uniform fine grid, respectively. We also plot in Fig. 24 the time evolution of the grid number ratio between the AMR and uniform fine grid resolutions. Besides little fluctuations inherent to discrete numerical methods, the general trend is an increase with time as the fluid volume expands. It must be reminded that, in our simulation case, the concentration gradient is essentially important near the dissolving interface, in the absence of large convective phenomena like salt fingering. If such instabilities would occur, the AMR algorithm could lead to mesh refining in the fluid volume and reduction of the efficiency.

6. Conclusion

To solve efficiently for the cavity dissolution problems, we proposed to use a porous medium based diffuse interface method for the modeling, combining with an adaptive mesh refinement method to reduce the gridblocks. Numerical examples were performed on two-dimensional examples to validate the modeling and the computation by comparing with other software calculations. A full three-dimensional core-scale example and a reservoir scale example were carried out to study the behavior of the moving dissolution front, as well as the mass transport. The DIM model with the AMR method is found to be able to capture the natural convection patterns (salt fingering) arising in some physical configurations, thanks to the refinement criterion based on the mass fraction variation. We also found out that the tube configuration could not generate as strong physical instability as the channel under the same condition, due to stabilizing effect induced by lateral dissolution. The proposed AMR method is shown to be very attractive in terms of computational time, while maintaining a good degree of accuracy. The DIM method as well as the computational skills will be further improved in the future along several lines. Gas phase and multi-component systems will be considered in order to handle more complex dissolution problems, e.g., carbonate dissolution, CO₂ storage. Higher order schemes for the transport equations as well as better ODE solvers will be developed. Other momentum equations, like the Darcy–Brinkman equation, will be to try. Parallelization will also be added.

Appendix. A novel numerical scheme to calculate the interfacial velocity on the AMR grid

First we perform an integration of the pressure along the path from the cell-center point ($P_{i,j}$ in Fig. 2 for instance) to the auxiliary point ($P_{i,j;en}$ in Fig. 2 for instance) with the help of Darcy's Law. Here, e is short for east and n is short for north; and so forth. Then, the velocity flux on the interface ($u_{i,j;en}$ in Fig. 2 for instance) is computed by the pressure difference of this new point and its neighbor cell-center point ($P_{i,j;EN}$ in Fig. 2 for instance) using Darcy's Law. Details are given in the following. Let us consider the case that the actual grid block connects with two fine gridblocks to the east side (see Fig. 2). Then the velocity at the interface of the actual gridblock (i, j) and the upper gridblock is represented by $u_{i,j;en}$, and we use the notation $u_{i,j;es}$ for the case of the lower

gridblock. The actual coarse gridblock is subdivided into 4 sub-blocks. We assume that the velocity is uniform over each sub-blocks, for example, sub-block i, j ; en has uniform velocities $u_{i,j;en}$ and $v_{i,j;ne}$ along the x - and y -axis, respectively. According to Eq. (13), we have

$$\nabla P = \rho \mathbf{g} - \mu_l^* K^{-1} \mathbf{V}. \quad (\text{A.1})$$

In the above equation, we assume the permeability tensor \mathbf{K} is isotropic, $\mathbf{K} = K\mathbf{I}$, and the permeability K is a function of ε_l given by Eq. (14). Neglecting the variations of ρ , μ_l^* and ε_l in a coarse cell, we integrate Eq. (A.1) from location m to n to obtain the following expression

$$P_m^n = \int_m^n (\rho \mathbf{g} - \mu_l^* K^{-1} \mathbf{V}) \cdot d\mathbf{l} \quad (\text{A.2})$$

where P_m^n represents the pressure difference between point n and point m , and \mathbf{l} represents the path vector.

If m represents the location of $P_{i,j}$ and n the location of $P_{i,j;en}$, then the integration path can be represented by the blue arrows depicted in Fig. 2. As a result, Eq. (A.2) can be written as

$$P_{i,j;en} = P_{i,j} + (\rho g_x - \mu_l^* K^{-1} u_{i,j;en}) \Delta x_{i,j}/4 + (\rho g_y - \mu_l^* K^{-1} v_{i,j;ne}) \Delta y_{i,j}/4 \quad (\text{A.3})$$

where $\Delta x_{i,j}$ and $\Delta y_{i,j}$ are the length of the actual grid along the x - and y -axis, respectively.

Using Eq. (13) the velocities are then given by

$$u_{i,j;en} = - \left(\frac{K}{\mu_l^*} \right)_{i,j;en} \left(\frac{P_{i,j;en} - P_{i,j}}{\Delta x_{i,j}/2} - [\rho g_x]_{i,j} - \frac{2 \left(\rho g_x - \mu_l^* K^{-1} u_{i,j;en} \right) \Delta x_{i,j} + \left(\rho g_y - \mu_l^* K^{-1} v_{i,j;ne} \right) \Delta y_{i,j}}{2 \Delta x_{i,j}} \right) \quad (\text{A.4})$$

where $u_{i,j;en}^*$ and $v_{i,j;ne}^*$ represent the velocity values of the converged Newton step, and $\left(\frac{K}{\mu_l^*} \right)_{i,j;en}$ is the harmonic average of the values of the two cells. Finally, we are able to compute the velocity fluxes at the interfaces with the help of the numerical integrations presented above.

References

- [1] S. Pandey, A. Chaudhuri, S. Kelkar, V. Sandeep, H. Rajaram, Investigation of permeability alteration of fractured limestone reservoir due to geothermal heat extraction using three-dimensional thermo-hydro-chemical (THC) model, *Geothermics* 51 (2014) 46–62.
- [2] P. Gamazo, S. Bea, M. Saaltink, J. Carrera, C. Ayora, Modeling the interaction between evaporation and chemical composition in a natural saline system, *J. Hydrol.* 401 (3) (2011) 154–164.
- [3] J.P. Crawshaw, E.S. Boek, Multi-scale imaging and simulation of structure, flow and reactive transport for CO₂ storage and eor in carbonate reservoirs, *Rev. Mineral. Geochem.* 77 (1) (2013) 431–458.
- [4] B. Ren, Y. Xu, S. Ren, X. Li, P. Guo, X. Song, et al., Laboratory assessment and field pilot of near miscible CO₂ injection for ior and storage in a tight oil reservoir of Shengli Oilfield China, in: *SPE Enhanced Oil Recovery Conference*, Society of Petroleum Engineers, 2011.
- [5] P. Négrel, R. Millot, E. Petelet-Giraud, E. Malcuit, A. Brenot, Impact of rock weathering on the chemical composition of groundwater determined by inverse modeling in large sedimentary basins, *Procedia Earth Planet. Sci.* 7 (2013) 615–619.
- [6] H. Luo, F. Laouafa, J. Guo, M. Quintard, Numerical modeling of three-phase dissolution of underground cavities using a diffuse interface model, *Int. J. Numer. Anal. Methods Geomech.* 38 (2014) 1600–1616. <http://dx.doi.org/10.1002/nag.2274>.
- [7] J. De Waele, L. Plan, P. Audra, Recent developments in surface and subsurface karst geomorphology: an introduction, *Geomorphology* 106 (2009) 1–8.
- [8] M. Ezersky, A. Frumkin, Fault–dissolution front relations and the Dead Sea sinkhole problem, *Geomorphology* 201 (2013) 35–44.
- [9] A. Zidane, E. Zechner, P. Huggenberger, A. Younes, Simulation of rock salt dissolution and its impact on land subsidence, *Hydrol. Earth Syst. Sci. Discuss.* 10 (10) (2013) 12255–12291.
- [10] S. Whitaker, *The Method of Volume Averaging*, Kluwer Academic Publishers, Dordrecht, The Netherlands, 1999.
- [11] M. Quintard, S. Whitaker, Convection, dispersion, and interfacial transport of contaminant: homogeneous porous media, *Adv. Water Resour.* 17 (1994) 221–239.
- [12] M. Quintard, S. Whitaker, Dissolution of an immobile phase during flow in porous media, *Ind. Eng. Chem. Res.* 38 (1999) 833–844.
- [13] J. Chadam, D. Hoff, E. Merino, P. Ortoleva, A. Sen, Reactive infiltration instabilities, *IMA J. Appl. Math.* 36 (1986) 207–221.
- [14] X. Liu, A. Ormond, K. Bartko, Y. Li, P. Ortoleva, A geochemical reaction-transport simulator for matrix acidizing analysis and design, *J. Pet. Sci. Eng.* 17 (1997) 181–196.
- [15] F. Golfier, C. Zarcone, B. Bazin, R. Lenormand, D. Lasseux, M. Quintard, On the ability of a darcy-scale model to capture wormhole formation during the dissolution of a porous medium, *J. Fluid Mech.* 457 (2002) 213–254.
- [16] C. Oltéan, F. Golfier, M.A. Buès, Numerical and experimental investigation of buoyancy-driven dissolution in vertical fracture, *J. Geophys. Res. Solid Earth* 118 (5) (2013) 2038–2048.
- [17] J. Donea, S. Giuliani, J. Halleux, An arbitrary Lagrangian–Eulerian finite element method for transient dynamic fluid–structure interactions, *Comput. Methods Appl. Mech. Engrg.* 33 (1982) 689–723.
- [18] Y. Amini, H. Emdad, M. Farid, A new model to solve fluid–hypo-elastic solid interaction using the smoothed particle hydrodynamics (SPH) method, *Eur. J. Mech. B Fluids* 30 (2) (2011) 184–194.
- [19] W. Sun, G. Liu, L. Wang, T. Wu, Y. Liu, An arbitrary Lagrangian–Eulerian model for studying the influences of corrosion product deposition on bimetallic corrosion, *J. Solid State Electrochem.* 17 (3) (2013) 829–840.
- [20] L. Chen, Q. Kang, B. Carey, W.-Q. Tao, Pore-scale study of diffusion– processes involving dissolution and precipitation using the lattice Boltzmann method, *Int. J. Heat Mass Transfer* 75 (2014) 483–496.
- [21] L. Chen, Q. Kang, B.A. Robinson, Y.-L. He, W.-Q. Tao, Pore-scale modeling of multiphase reactive transport with phase transitions and dissolution–precipitation processes in closed systems, *Phys. Rev. E* 87 (4) (2013) 043306.
- [22] Z. Xu, H. Huang, X. Li, P. Meakin, Phase field and level set methods for modeling solute precipitation and/or dissolution, *Comput. Phys. Comm.* 183 (1) (2012) 15–19.
- [23] G. Vignoles, Y. Aspa, M. Quintard, Modelling of carbon–carbon composite ablation in rocket nozzles, *Compos. Sci. Technol.* 70 (9) (2010) 1303–1311.
- [24] C.W. Hirt, B.D. Nicolas, Volume of fluid (VOF) method for the dynamics of free boundaries, *J. Comput. Phys.* 39 (1981) 201–225.
- [25] J. Sethian, P. Smereka, Level set methods for fluid interfaces, *Annu. Rev. Fluid Mech.* 35 (2003) 341–372.
- [26] T. Van Noorden, Crystal precipitation and dissolution in a porous medium: effective equations and numerical experiments, *Multiscale Model. Simul.* 7 (3) (2009) 1220–1236.
- [27] V. Clément, V.M. Tan, B. Samir, A. Pierre, Reactive transport in porous media: pore-network model approach compared to pore-scale model, *Phys. Rev. E* 87 (2) (2013) 023010.
- [28] J.B. Collins, H. Levine, Diffuse interface model of diffusion-limited crystal growth, *Phys. Rev. B* 31 (1985) 6119–6122.
- [29] C. Beckermann, H.-J. Diepers, I. Steinbach, A. Karma, X. Tong, Modeling melt convection in phase-field simulations of solidification, *J. Comput. Phys.* 154 (1999) 468–496.
- [30] Z. Xu, P. Meakin, Phase-field modeling of solute precipitation and dissolution, *J. Chem. Phys.* 129 (2008) 014705.
- [31] H. Luo, M. Quintard, G. Debenest, F. Laouafa, Properties of a diffuse interface model based on a porous medium theory for solid–liquid dissolution problems, *Comput. Geosci.* 16 (4) (2012) 913–932.
- [32] C. Maisons, E. Fortier, M. Valette, Induced microseismicity and procedure for closure of brine production caverns, in: *Seismicity Associated with Mines, Reservoirs and Fluid Injections*, Springer, 1998, pp. 585–603.
- [33] D. Raucoules, C. Maisons, C. Carnec, S. Le Mouelic, C. King, S. Hosford, Monitoring of slow ground deformation by ERS radar interferometry on the Vauvert salt mine (France): comparison with ground-based measurement, *Remote Sens. Environ.* 88 (4) (2003) 468–478.
- [34] M.J. Berger, P. Colella, Local adaptive mesh refinement for shock hydrodynamics, *J. Comput. Phys.* 82 (1989) 64–84.
- [35] H. Zhang, Z. Chen, B. Li, X. Jiang, The secondary vortex rings of a supersonic underexpanded circular jet with low pressure ratio, *Eur. J. Mech. B Fluids* 46 (2014) 172–180.
- [36] G.S.H. Pau, J.B. Bell, A.S. Almgren, K.M. Fagnan, M.J. Lijewski, An adaptive mesh refinement algorithm for compressible two-phase flow in porous media, *Comput. Geosci.* 16 (2012) 577–592.
- [37] P. Durbin, G. Iaccarino, An approach to local refinement of structured grids, *J. Comput. Phys.* 181 (2) (2002) 639–653.
- [38] B.N. Chetverushkin, N.G. Churbanova, M.A. Trapeznikova, A.A. Sukhinov, A.A. Malinovskij, Adaptive Cartesian mesh refinement for simulating multiphase flows in porous media, *Comput. Methods Appl. Math.* 8 (2008) 101–115.
- [39] M. Gerritsen, J.V. Lambers, Integration of local–global upscaling and grid adaptivity for simulation of subsurface flow in heterogeneous formations, *Comput. Geosci.* 12 (2008) 193–208.
- [40] G. Scovazzi, A. Gerstenberger, S. Collis, A discontinuous Galerkin method for gravity-driven viscous fingering instabilities in porous media, *J. Comput. Phys.* 233 (2013) 373–399.

- [41] P. Forsyth, P. Sammon, Practical considerations for adaptive implicit methods in reservoir simulation, *J. Comput. Phys.* 62 (2) (1986) 265–281.
- [42] M. Mamaghani, G. Enchery, C. Chainais-Hillairet, Development of a refinement criterion for adaptive mesh refinement in steam-assisted gravity drainage simulation, *Comput. Geosci.* 15 (2011) 17–34.
- [43] C. Rendleman, V. Beckner, M.J. Lijewski, W. Crutchfield, J. Bell, Parallelization of structured, heirarchical adaptive mesh refinement algorithms, *Comput. Vis. Sci.* 3 (3) (2000) 147–157.
- [44] R.D. Hornung, A.M. Wissink, S.R. Kohn, Managing complex data and geometry in parallel structured AMR applications, *Eng. Comput.* 22 (2006) 181–195.
- [45] F.A. Coutelieres, M.E. Kainourgiakis, A.K. Stubos, E.S. Kikkinides, Y.C. Yortsos, Multiphase mass transport with partitioning and inter-phase transport in porous media, *Chem. Eng. Sci.* 61 (14) (2006) 4650–4661.
- [46] C. Soulaire, G. Debenest, M. Quintard, Upscaling multi-component two-phase flow in porous media with partitioning coefficient, *Chem. Eng. Sci.* 66 (2011) 6180–6192.
- [47] C. Zheng, G.D. Bennett, *Applied Contaminant Transport Modeling: Theory and Practice*. Vol. 440, Van Nostrand Reinhold, New York, 1995.
- [48] C. Zhao, T. Poulet, K. Regenauer-Lieb, B. Hobbs, Computational modeling of moving interfaces between fluid and porous medium domains, *Comput. Geosci.* 17 (1) (2013) 151–166.
- [49] P. Angot, C.-H. Bruneau, P. Fabrie, A penalization method to take into account obstacles in incompressible viscous flows, *Numer. Math.* 81 (4) (1999) 497–520.
- [50] R.D. Hornung, J.A. Trangenstein, Adaptive mesh refinement and multilevel iteration for flow in porous media, *J. Comput. Phys.* 136 (1997) 522–545.
- [51] O. Schenk, K. Gärtner, Solving unsymmetric sparse systems of linear equations with pardiso, *Future Gener. Comput. Syst.* 20 (3) (2004) 475–487.
- [52] P.E. Dijk, B. Berkowitz, Buoyancy-driven dissolution enhancement in rock fractures, *Geology* 28 (2000) 1051–1054.
- [53] P.E. Dijk, B. Berkowitz, Y. Yechieli, Measurement and analysis of dissolution patterns in rock fractures, *Water Resour. Res.* 38 (2002) <http://dx.doi.org/10.1029/2001WR000246>.